WILEY-VCH

# Synergistic Regulation of Nickel Doping/Hierarchical Structure in Cobalt Sulfide for High Performance Zinc-Air Battery

*Jie Wang, Jinxiao Xu, Xunyun Guo, Tao Shen, Cuijuan Xuan, Baoling Tian, Zhaorui Wen, Ye Zhu* and Deli Wang**

Prof. J. Wang, Ms. J. X. Xu, Prof. C. J. Xuan, Dr. B. L. Tian,
College of Chemistry and Pharmaceutical Sciences, Qingdao Agricultural University, Qingdao, 266109, China.

Dr. X. Y. Guo, Prof. Y. Zhu
*Department of Applied Physics, Research Institute for Smart Energy, The Hong Kong Polytechnic University, Hung Hom, Hong Kong, China.*
E-mail: ye.ap.zhu@polyu.edu.hk

Dr. T. Shen, Prof. D. L. Wang
Key Laboratory of Material Chemistry for Energy Conversion and Storage (Huazhong University of Science and Technology), Ministry of Education, Hubei Key Laboratory of Material Chemistry and Service Failure, School of Chemistry and Chemical Engineering, Huazhong University of Science and Technology, Wuhan, 430074, P.R. China.
E-mail: wangdl81125@hust.edu.cn

Dr. Z. R. Wen
Joint Key Laboratory of the Ministry of Education, Institute of Applied Physics and Materials Engineering (IAPME), University of Macau, Macau SAR, China.

**Keywords:** nickel doped $Co_9S_8$, hierarchical porous structure, synergistic regulation, oxygen reduction/evolution reaction, Zn-air battery

**Abstract:** Exploring efficient bi-functional oxygen electrocatalysts with spatially hierarchical architecture, high electrical conductivity and superior intrinsic activity is essential for high performance Zn-air batteries. In this paper, we present reduced-graphene-nanoribbon supported nickel doped $Co_9S_8$ nanoparticles (Ni-$Co_9S_8$/rGN) via a simple solvothermal procedure for the electrocatalysis of oxygen reduction and evolution reactions. Such composite assembled by spindle-type nanorods to form a spherical hierarchical structure features high surface area and good hydrophilicity property. Excellent OER/ORR activities and long-term stabilities are obtained on Ni-$Co_9S_8$/rGN relative to $RuO_2$ and Pt/C. Density functional theory (DFT) calculations demonstrate that the nickel dopants in the $Co_9S_8$ structure effectively optimizes the adsorption properties at the rate-determining steps during ORR/OER processes. Therefore, the superior catalytic performance is ascribed to the synergistic regulation between the uniform rGN covered hierarchical structure and nickel dopants by promotes the intrinsic ORR/OER properties, electrical conductivity, and mass transfer. Moreover, as a bi-functional catalyst for the rechargeable and flexible Zn–air batteries, excellent battery performance are achieved, including high power density, superior rate performance and long-term cycling stability, providing a promising avenue for high-efficiency catalysts in energy conversion.

## 1. Introduction

In order to meet the ever increasing requirement of energy for the modernization needs and decrease the adverse effect of fossil fuels to the environment, renewable energy-related devices, like fuel cells, lithium ion batteries, metal-air batteries, etc., are under extensive investigation because of their numerous merits (e.g., environmental friendly, high-mobility and high energy density), which have been recognized as substitute for the traditional energy resources.[1-3] Among them, the Zn–air battery is a kind of device operated in alkaline electrolytes, which possesses high theoretical mass energy density of 1320 Wh $kg^{-1}$ and can

provide ultra-stable discharge potential. It should be noted that high-efficiency oxygen reduction reaction (ORR) and oxygen evolution reaction (OER) catalytic activity is essential at the cathode, which held back the practical application in social life and appeals for efficient catalyst to boost their sluggish reaction kinetics.[4-6] To date, Pt/C and its alloy catalysts are reckoned as the most active catalysts for ORR, while $IrO_2$ and $RuO_2$ are responsible for high performance OER.[7-10] These catalysts, however, suffer from demerits of scarcity in resources, high cost, low stability when operating and most importantly possess single-functionalized catalytic activity (ORR or OER), greatly limited their further application.[11-14] Therefore, the exploration of bi-functional catalysts to drive both the ORR and OER is necessary for the improvement of the overall performance of a Zn–air battery.

*3d* transition metal based materials have been extensively investigated due to their earth abundance and low-cost advantages, especially for the oxides,[15-17] nitrides,[18-20] sulfides[21-23] and dihydroxides.[24-26] Among them, transition metal chalcogenides have attracted particular interests for their rich redox chemistry which contributes to intrinsic active sites in electrochemical reactions,[27-29] especially for the ORR and OER. Besides, they characterize higher electrical conductivity relative to transition metal oxides, and oxygen tolerance compared with metal alloys, phosphides and carbides.[30] More recently, $Co_9S_8$ has aroused intense attention in the energy field because that $Co_9S_8$ characterizes more Co-rich components which are often assigned to the active center for electrocatalysis.[30-32] Since the electrochemical activities generally occur on the microchemical interface of the catalyst, hence, tuning the morphology, introducing dopants or substrates, functional modifications and coordinating with high-electrical conductivity carbon support are efficient ways to further improve the electrocatalytic properties of $Co_9S_8$.[33-35] Therefore, novel and rational strategies are appealing to improve the catalytic activities of the $Co_9S_8$ based catalysts to meet the requirements of superior ORR/OER and practical Zn–air battery applications.

In this work, applying reduced-graphene-nanoribbon (rGN) as an electronic conductor, we report nickel doped $Co_9S_8$ nanocomposites (Ni-$Co_9S_8$/rGN) via a simple solvothermal procedure for the electrocatalysis of oxygen reduction/evolution reactions and Zn-air batteries. The hydrophilic composite features hierarchical structure with open porous structure and uniform graphene nanoribbon coverage, which effectively shortens the ion diffusion pathway and enhances the electron transfer rate. Excellent OER and ORR activities are obtained for Ni-$Co_9S_8$/rGN, which outperform other comparative samples. Combined with the DFT calculation, the superior catalytic performance towards ORR and OER is ascribed to the synergistic regulation between rGN covered uniform hierarchical structure and the Ni doping. When serving as a bi-functional catalyst for the rechargeable and flexible Zn–air batteries, excellent battery performances are achieved, outperforms commercial Pt/C+$RuO_2$ mixture catalysts.

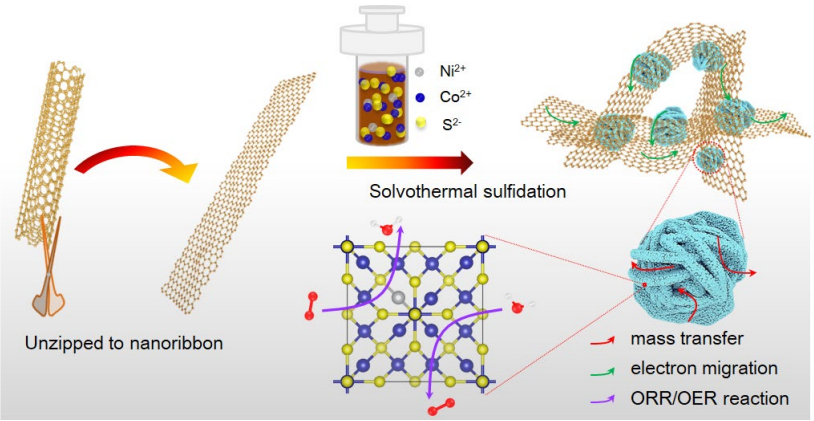


**Scheme 1**. Schematic illustration of the synthetic procedure of hierarchical structured Ni-$Co_9S_8$/rGN nanocomposites.

## 2. Results and Discussion

As illustrated in scheme 1, the hierarchical porous structured Ni-$Co_9S_8$/rGN was synthesized via a simple solvothermal approach (Scheme 1), in which the graphene nanoribbon served as electronic conductor was obtained by exfoliation of MWCNTs.[36, 37] The as-prepared products were characterized via Powder X-ray diffraction (XRD) in order to authenticate the specific crystal phase and purity. As can be seen from Fig. 1a, diffraction

peaks located at 15.4°, 29.8°, 31.2°, 39.5°, 47.6° and 52.1° corresponds to the (111), (311), (222), (331), (511) and (440) of $Co_9S_8$ (PDF # 03-065-1765), respectively. Obviously, there are no crystalline phases of Ni-based compounds in the Ni-$Co_9S_8$/rGN. Combining with XRD of Figure 1a and Figure S1, the catalyst without adding Co content features NiS/$Ni_9S_8$ composite phase (PDF # 00-012-0041 and 00-022-1193). The thermostability of the as-prepared catalysts was investigated via thermogravimetric analysis (TGA) in air (Figure S2), and the weight loss at temperature up to ~420 ℃ was attributed to the combustion of rGN, while further weight loss at high temperature of ~680 ℃ was assigned to the phase transformation from metal sulfides to metal oxides.

The microstructure of the as-prepared catalysts was characterized by SEM and TEM techniques. Typical for Ni-$Co_9S_8$/rGN, obvious hierarchical spherical structure can be seen from the SEM image (Figure 1b), in which the spheres were assembled by numerous spindle-type nanorods. Although the specific sphere size is at the micro-scale, the nanorods are ~100 nm in diameter and ~200 nm in length. Such unique structure would play key roles in increasing the electrochemically active interfaces, enhancing the cycling stability, and then improving the overall performance of electrode for electrochemical reactions. The high-angle annular dark-field scanning transmission electron microscopy (HAADF-STEM) image of Ni-$Co_9S_8$/rGN (Figure 1c) showed that the spheres feature porous structure and large surface area, which are in favor of ion transport in the catalytic process, and can effectively increase the electrochemically active interface. For comparison, the specific morphologies of Ni-$Co_9S_8$, $Co_9S_8$/rGN and NiS/$Ni_9S_8$/rGN samples were also characterized (Figure S3). The hierarchical morphology was largely maintained for $Co_9S_8$/rGN, in contrast to much compact Ni-$Co_9S_8$ and bulk-like NiS/$Ni_9S_8$/rGN. In order to precisely investigate the porosity of the as-prepared catalysts, $N_2$ adsorption measurements were conducted. As depicted in Figure S4a, the nitrogen adsorption isotherm of Ni-$Co_9S_8$/rGN exhibits a clear hysteresis loop at $P/P_0$ value of near 1, indicating the existence of mesoporous and macroporous structure of the samples.[38-40]

As a result, the corresponding BET surface area of Ni-$Co_9S_8$/rGN is 109.7 $m^2 g^{-1}$, which is larger than Ni-$Co_9S_8$ (18.6 $m^2 g^{-1}$), $Co_9S_8$/rGN (92.8 $m^2 g^{-1}$) and NiS/$Ni_9S_8$/rGN (55.4 $m^2 g^{-1}$), but smaller than rGN (313.9 $m^2 g^{-1}$). The wide pore size distribution of Ni-$Co_9S_8$/rGN (Figure S4b) further confirmed the hierarchical architecture.

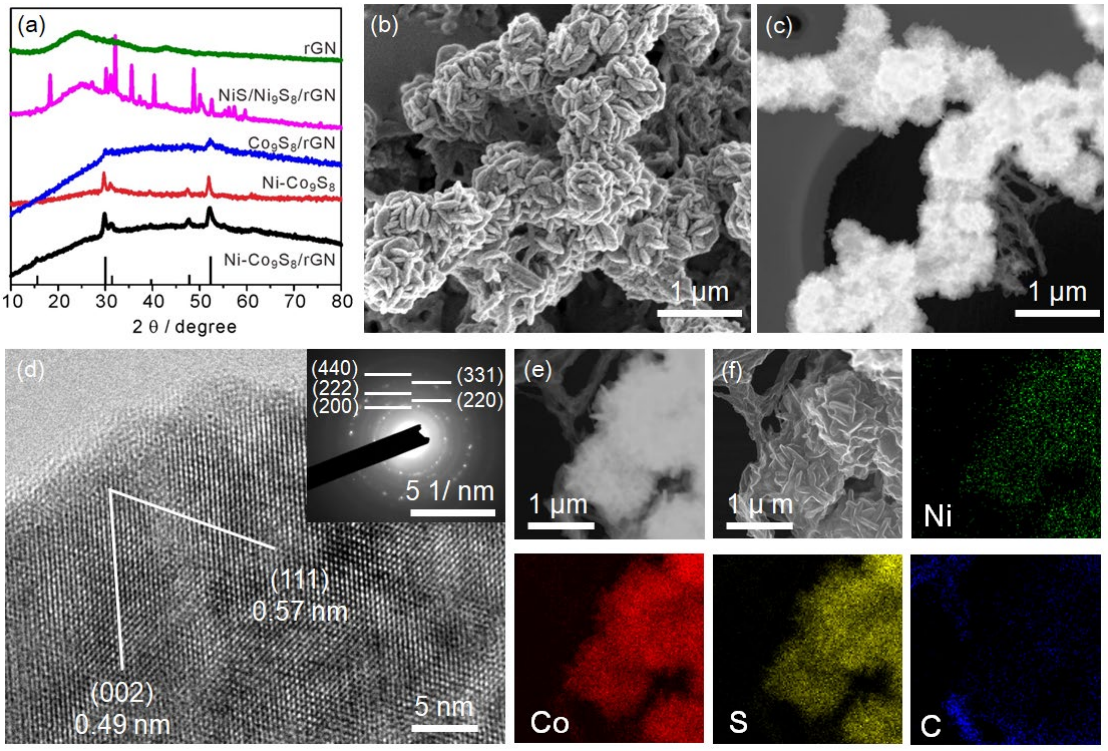


**Figure 1 The phase, morphology, micro-structure and elemental distribution information.** (a) XRD patterns of Ni-$Co_9S_8$/rGN, Ni-$Co_9S_8$, $Co_9S_8$/rGN, NiS/$Ni_9S_8$/rGN and rGN materials; (b) SEM image of Ni-$Co_9S_8$/rGN; (c) HAADF-STEM image of Ni-$Co_9S_8$/rGN; (d) HRTEM image of Ni-$Co_9S_8$/rGN and the corresponding SAED pattern (inset); (e) Enlarged HAADF-STEM image of Ni-$Co_9S_8$/rGN, the corresponding backscattered electron image (f) and EDS maps of Ni, Co, S, C elements.

High resolution TEM (HRTEM) was conducted for part of a Ni-$Co_9S_8$/rGN particle, which showed obvious lattice fringes with inter-planar spacing of ~0.57 and 0.49 nm from the two orientations, corresponding to the (111) and (002) planes, respectively. The fitted selected area electron diffraction (SAED) pattern displayed characteristic diffraction rings, representing (200), (220), (222), (331) and (440) planes from the inside out, respectively. Therefore, the XRD, HRTEM and SAED results all revealed the high-quality crystal structure of $Co_9S_8$ in Ni-$Co_9S_8$/rGN. As for Ni-$Co_9S_8$, $Co_9S_8$/rGN and NiS/$Ni_9S_8$/rGN samples, the corresponding HRTEM images and SAED patterns (Figure S5) also show high-quality crystal

structure. It should be noted from the backscattered STEM image in Figure 1f that graphene nanosheets covered the Ni-$Co_9S_8$ particles compared with the HAADF-STEM image (Figure 1e) at the same position. The uniform and ultrathin carbon coverage would effectively enhance the electrical conductivity and then accelerate the electron transfer rate, which is beneficial to the catalytic activities. EDS mapping was performed to investigate the composition of Ni-$Co_9S_8$/rGN, in which the particle showed uniform distribution of Ni, Co and S, with thin carbon coverage on the surface. It should be noted that the Ni content characterized by EDS in the sphere is ultralow (1.2%, Figure S6 and Table S1), demonstrating that Ni was successfully doped in the $Co_9S_8$ particle. EDS characterization on other samples was also performed (Figure S7-S9) and confirmed the existence of uniform elemental distribution of Ni, Co, S and C species.

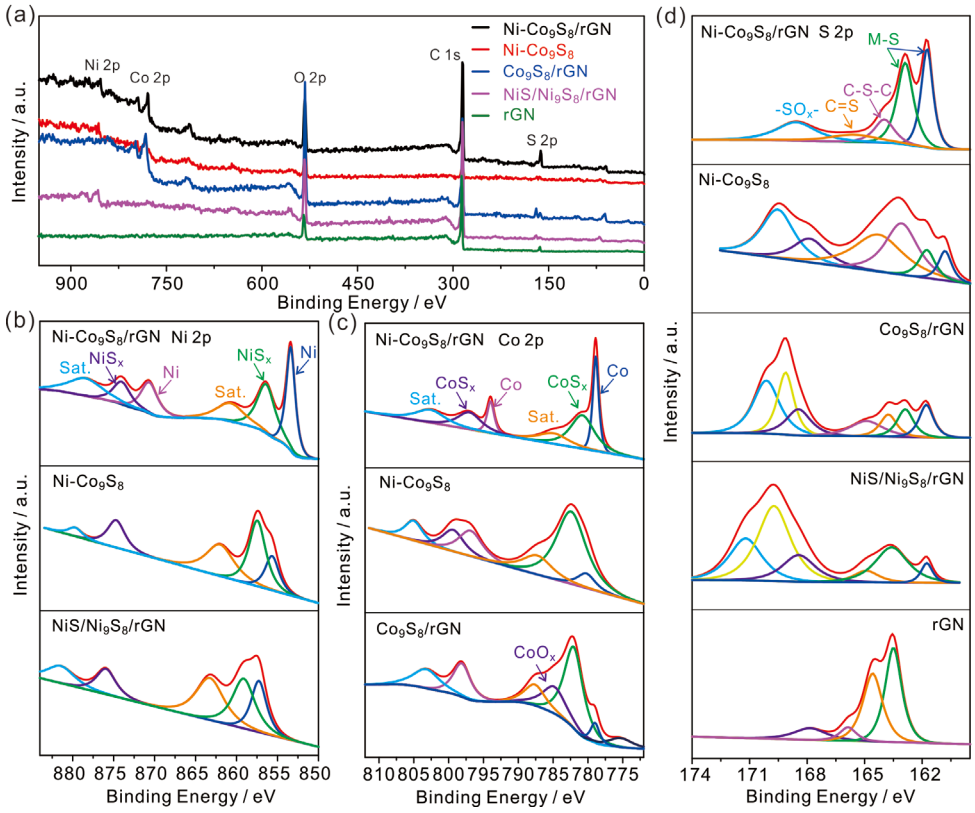


**Figure 2 XPS characterization of the as-prepared catalysts.** (a) Full-range spectrum of Ni-$Co_9S_8$/rGN, Ni-$Co_9S_8$, $Co_9S_8$/rGN, NiS/$Ni_9S_8$/rGN and rGN materials; (b) high-resolution Ni 2p spectrum of Ni-$Co_9S_8$/rGN, Ni-$Co_9S_8$ and NiS/$Ni_9S_8$/rGN; (c) high-resolution Co 2p spectrum of Ni-$Co_9S_8$/rGN, Ni-$Co_9S_8$ and $Co_9S_8$/rGN; (d) high-resolution S 2p spectrum of Ni-$Co_9S_8$/rGN, Ni-$Co_9S_8$, $Co_9S_8$/rGN, NiS/$Ni_9S_8$/rGN and rGN.

Further information related to the chemical states of the samples were analyzed through the core-level XPS technique and fitted by a Gaussian fitting scheme. The surface survey XPS spectra of the samples (Figure 2a) demonstrated the existence of Ni 2p, Co 2p, O 2p, C 1s and S 2p signals which are located at near binding energies of 853.5, 778.5, 530.0, 286.7 and 162.3 eV respectively.[41] The existence of C signal for Ni-$Co_9S_8$ sample may be ascribed to the carbonization of TAA during the synthetic process. The fitted high-resolution Ni 2p spectra (Figure 2b) of Ni-$Co_9S_8$/rGN, Ni-$Co_9S_8$ and NiS/$Ni_9S_8$/rGN demonstrated the characteristic peaks of Ni, $NiS_x$ and satellite peak.[42-45] In the high-resolution Co 2p spectrum, the characteristic peaks of Co $2p_{3/2}$ and Co $2p_{1/2}$ are clearly seen. Typical for Ni-$Co_9S_8$/rGN sample, the spectrum is decomposed into six peaks (Figure 2c). Among them, peaks located at 785.2 and 802.6 eV represent the satellite peaks due to the shakeup excitation of the high-spin $Co^{2+}$, peaks at 778.7 and 794.0 eV correspond to the $Co^0$ species, and peaks at 781.0 and 797.3 eV represent the $CoS_x$ species.[46-48] The high-resolution S2p spectra (Figure 3b) of the five samples exhibit three kinds of S species, one is the metal–S bonds located at 161.8 and 162.8 eV, revealing the successful synthesis of metal sulfides, another is the C–S–C bond (163.9 eV) and C=S bond (165.5 eV), illustrating that part of S elements is doped in the carbon framework, and the rest peaks represent the $–SO_x–$ species at higher binding energies.[37, 49] To be noted, the metal–S bonds shifted to the higher binding energy after unified with rGN compared with the Ni-$Co_9S_8$ sample, indicating high physical interaction between Ni-$Co_9S_8$ and the rGN support. The hydrophilicity properties of the as-prepared samples were investigated by measuring the contact angle in water media. In detail, the contact angle for Ni-$Co_9S_8$/rGN is 35.9° (Figure S10), much lower than the samples of $Co_9S_8$/rGN (46.1°), Nis-$Ni_9S_8$/rGN (51.1°), Ni-$Co_9S_8$ (62.3), rGN (47.0°), Pt/C (66.7°), and $RuO_2$ (47.3°), revealing the excellent hydrophilic property. The high hydrophilicity of Ni-$Co_9S_8$/rGN relative to pure Ni-$Co_9S_8$ and rGN may be ascribed to the optimization of the morphology of metal sulfides by introducing rGN and the existence of interfaces between Ni-

$Co_9S_8$ and rGN. The excellent hydrophilicity is in favor of the intimate contact between water electrolyte and electrode, maximizes the active surface area, and accelerates the reaction kinetics accordingly.

To evaluate the electrochemical performance of ORR and OER, the electrocatalytic measurements of the as-prepared catalysts were conducted in alkaline electrolytes. The ORR polarization curves of the Ni-$Co_9S_8$/rGN (Figure 3a) shows an onset potential and a half-wave potential ($E_{1/2}$) of 0.98 V and 0.83 V, respectively, which were more positive than Ni-$Co_9S_8$ (0.88 and 0.76 V), $Co_9S_8$/rGN (0.87 and 0.75 V), NiS/$Ni_9S_8$/rGN (0.84 and 0.62 V) and rGN (0.81 and 0.54 V), close to those of Pt/C (1.01 and 0.85 V). The trend for the polarization curves agreed well with the cyclic voltammograms (CV) scans (Figure S11). Meanwhile, the polarization curves for the OER showed ultra-high activities of Ni-$Co_9S_8$/rGN (Figure 3b) with lower onset potential and polarization potential relative to the $RuO_2$ and other comparative catalysts. To determine the specific catalytic activities of the bi-functional catalysts, voltage gap ($\Delta E$) between the $E_{j=10\ mA\ cm\text{-}2}$ of OER and $E_{1/2}$ of ORR were drew out via a histogram (Figure 3c). As can be seen, the Ni-$Co_9S_8$/rGN achieved the lowest $\Delta E$ value of 0.65 V, which outperformed the Ni-$Co_9S_8$ (0.80 V), $Co_9S_8$/rGN (0.84 V), NiS/$Ni_9S_8$/rGN (1.01 V), rGN (1.15 V) and even the composite of Pt/C/$RuO_2$ (0.68 V). The electrochemical performance of Ni-$Co_9S_8$/rGN rated in the first row compared with many recent reported catalysts (Table S2). Therefore, it is preliminarily confirmed that Ni-doping in Ni-$Co_9S_8$/rGN played key roles in accelerating the bi-functional activities towards ORR and OER.

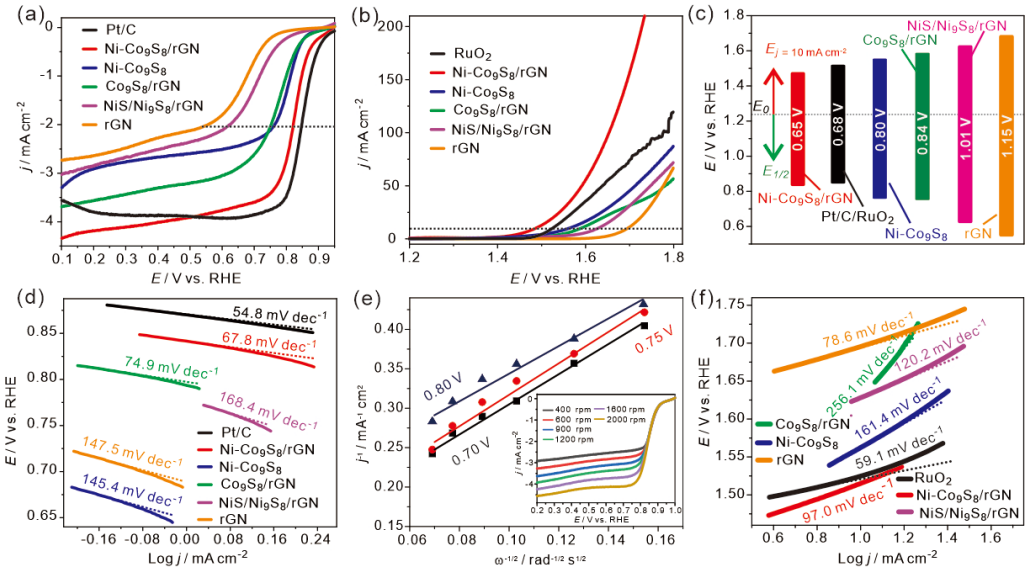


**Figure 3 The electrochemical activities and kinetics of the as-prepared catalysts.** LSV polarization curves for the ORR (a) and OER (b); (c) Histogram of the voltage gap between OER and ORR; (d) Tafel plots derived from (a); (e) LSV polarization curves for the ORR at different scanning rates (inset) and the corresponding K-L plots; (f) Tafel plots derived from (b).

The reaction kinetics of the ORR and OER were also studied for the as-prepared catalysts. As for ORR, Tafel plots (Figure 3d) derived from the polarization curves (Figure 3a) exhibited a smaller Tafel slope value (67.8 mV $dec^{-1}$) for the Ni-$Co_9S_8$/rGN than Ni-$Co_9S_8$ (145.4 mV $dec^{-1}$), $Co_9S_8$/rGN (74.9 mV $dec^{-1}$), NiS/$Ni_9S_8$/rGN (168.4 mV $dec^{-1}$), rGN (147.5 mV $dec^{-1}$), slight higher than Pt/C (154.8 mV $dec^{-1}$), demonstrating the fast reaction kinetics of Ni-$Co_9S_8$/rGN. The electron transfer kinetics of the ORR derived from the polarization measurements at different rotating rates (in set of Figure 3e) were further investigated. By increasing the rotating speed, the oxygen flux to the electrode surface would be enlarged, which resulted in the increasing values of limiting diffusion current density. The fitted Koutecky–Levich (K–L) plots of Ni-$Co_9S_8$/rGN at different potentials showed good linearity, suggesting the first-order reaction kinetics with respect to the concentration of dissolved oxygen.[50] Accordingly, the electron transfer number at the three potentials was calculated to be ~4.0, indicating a direct 4-electron transfer process. Moreover, polarization curves obtained via a rotating ring-disc electrode ($E_{ring}$ = 1.2 V vs. RHE) is described in Figure 3f. By deriving from the LSV curves (Figure S12), the $H_2O_2$ yield and electron transfer number

at potential ranging from 0.1 to 0.8 V was calculated to be ~6.9% and ~3.86 V respectively (Figure S13). Tafel plots (Figure 3f) derived from the OER polarization curves (Figure 3b) demonstrated that the Ni-$Co_9S_8$/rGN features relatively smaller slope value (97.0 mV $dec^{-1}$) than Ni-$Co_9S_8$ (161.4 mV $dec^{-1}$), $Co_9S_8$/rGN (256.1 mV $dec^{-1}$), and NiS/$Ni_9S_8$/rGN (120.2 mV $dec^{-1}$), and a bit higher than rGN (78.6 mV $dec^{-1}$) and $RuO_2$/C (59.1 mV $dec^{-1}$). The superior ORR and OER activities and reaction kinetics of Ni-$Co_9S_8$/rGN demostrates potential prospects in the application of metal-air batteries.

To obtain fundamental mechanistic insights into ORR and OER by Ni-doping in the $Co_9S_8$ structure, we performed first-principles density functional theory (DFT) calculations to study the reaction mechanisms. The theoretical models were built to illustrate the specific arrangement of Co and S atoms in a unit cell (Figure S14). Figure 4a shows the optimized models of stable adsorption configuration of ORR/OER intermediates (OOH*, O*, and OH*) on both catalysts. Free energy diagrams along reaction pathways were obtained using the scheme based on Nørskov et al.'s computational electrode model.[51] The OER path is shown below (Note: The ORR path can be regarded as the reverse of the following reactions, as reacted from $O_2$(g) to $H_2O$(l)):

$$H_2O(l) + * \leftrightarrow OH^* + H^+ + e^- \quad (1)$$

$$OH^* \leftrightarrow O^* + H^+ + e^- \quad (2)$$

$$H_2O(l) + O^* \leftrightarrow OOH^* + H^+ + e^- \quad (3)$$

$$OOH^* \leftrightarrow * + O_2(g) + H^+ + e^- \quad (4)$$

As can be seen from the free energy pathways of the four-electron ORR process in Figure 4b, all the electron transfer steps of Ni-$Co_9S_8$ electrode can be carried out spontaneously at a U value of below 0.51 V, indicating all reaction steps are exothermic. The whole process is dominated by the reaction step: $O_2(g) \rightarrow OOH^*$. For the pristine $Co_9S_8$, it was endothermic on the reaction step: $OH^* + H^+ + e^- = H_2O(l) + *$, at potential below 0.51 V. The results indicated higher electrochemical activity of the Ni-doped catalyst relative to pristine $Co_9S_8$. As for OER, the theoretical overpotential for spontaneous reaction of Ni-$Co_9S_8$ was 1.96 V (Figure 4c),

which pristine $Co_9S_8$ cannot reach, also demonstrating excellent OER activities of the Ni-$Co_9S_8$ electrode. Further DFT calculations of free energy pathways for the ORR/OER reaction processes on the two samples at 1.23 V illustrated the same results. Interestingly, the charge transfer from Ni substitution was confirmed by the DFT calculations (Figure S15). Therefore, Ni doping in the as-prepared catalysts effectively enhanced the intrinsic activities by decreasing $\Delta G$ at ORR/OER rate-determine steps, which was consistent with the experimental results, giving theoretical proof for superior ORR/OER catalytic activity resulting from Ni-doping in alkaline medium.

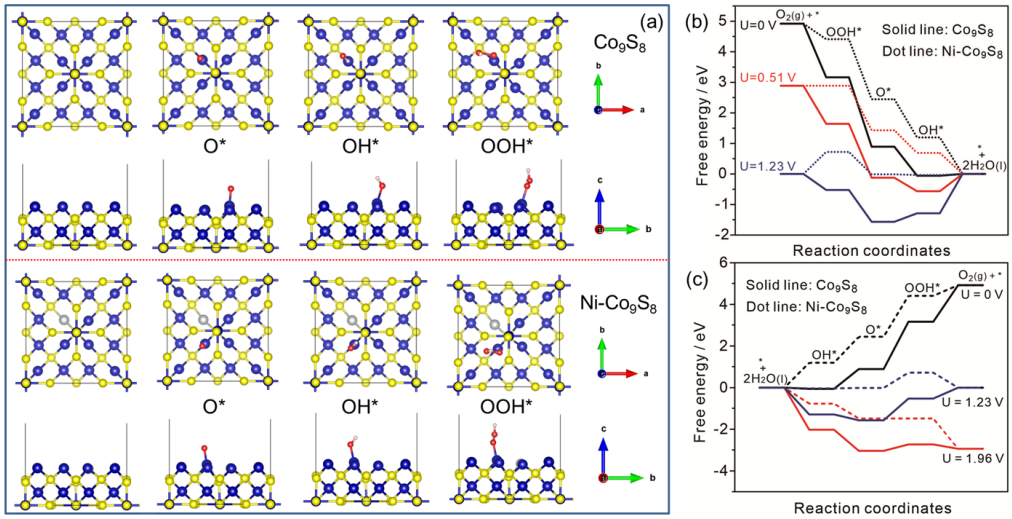


**Figure 4 DFT calculation of cubic centered $Co_9S_8$ and Ni-$Co_9S_8$.** (a) The models of pristine and stable adsorption configuration of OER/ORR intermediate (OOH*, O*, and OH*); (b) Free energy diagram of two models at different operation potentials for the ORR and OER.

Electrochemical specific surface area (ECSA) was investigated by measuring the CV curves at different scan rates were evaluated to determine the. According to the CV curves at the non-pseudocapacitance region (potential range of 0.10−0.30 V vs. RHE, inset of Figure 4a), the ECSA value of Ni-$Co_9S_8$/rGN was fitted and calculated to be 40.5 mF $cm^{-2}$, from the slope values of the linear plots of scan rate vs. the variation of charging current density ($\Delta j = j_a - j_c$) at 0.20 V. This value was higher than that of Ni-$Co_9S_8$ (2.3 mF $cm^{-2}$, Figure S16a), $Co_9S_8$/rGN (22.2 mF $cm^{-2}$, Figure S17), NiS/$Ni_9S_8$/rGN (14.6 mF $cm^{-2}$, Figure S18), and rGN (37.8 mF $cm^{-2}$, Figure S16b), indicating that the combined interaction of Ni-$Co_9S_8$ and rGN

effectively enhanced the electrochemically active area for ORR and OER. Additioanlly, the charge transfer kinetics of the as-prepared catalysts were analyzed by electrochemical impedance spectroscopy (EIS). The Nyquist plots in Figure 5b showed semicircles with different diameter for the four catalysts. After fitted via the equavalent circuit (inset of Figure 5c), Ni-$Co_9S_8$/rGN demonstrated much lower charge transfer resistance value (Figure 5c) relative to $Co_9S_8$/rGN and Ni-$Co_9S_8$, indicating that the Ni-doping and rGN support in the $Co_9S_8$ effectively enhanced the electrical conductivity. Therefore, the excellent bi-functional activity of Ni-$Co_9S_8$/rGN is mainly ascribed to the three following aspects: i, excellent Ni-doping structure effectively improved the electronic structure, and then improved the intrinsic activity; ii, the high specific surface area and good interaction between Ni-$Co_9S_8$ and rGN to form the hierarchical porous structure significantly enlarged the electrochemical interfaces; iii, the enhanced charge transfer caused by the coordination of rGN and Ni-doping.

Operation stability is another key parameter in practical application of the catalysts. Chronoamperometric tests (Figure 5d) at fixed potential of 0.70 V were adopted to determine the ORR stability, in which the Ni-$Co_9S_8$/rGN showed negligible current density loss even for 25k s (~ 7 h), while the Pt/C suffered gradual decrease of activity and only 68.4% of activity maintained at last. The OER stability was processed via a chronopotentiometry technique at a constant current density of 10 mA $cm^{-2}$ for over 300k s (~85 h, Figure 5d). As a result, Ni-$Co_9S_8$/rGN remained constant potential at ca. 1.48 V during the test, while $RuO_2$ started at 1.56 V and failed at 62k s. Therefore, the design of Ni-$Co_9S_8$/rGN effectively enhanced the activity and stability towards ORR and OER.

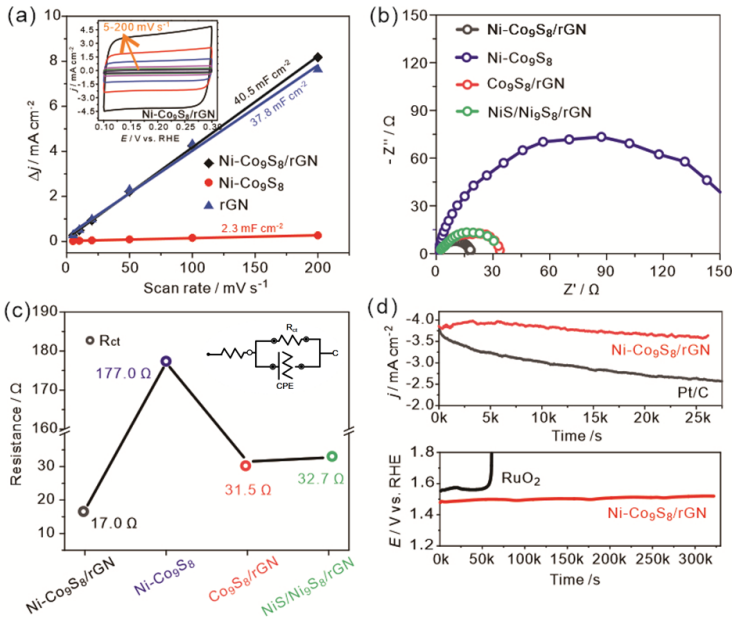


**Figure 5 The electrochemical properties of the as-prepared catalysts.** (a) CV curves of Ni-$Co_9S_8$/rGN at different scan rates (inset) and the linear plots of the scan rates vs. current density variation at 0.20 V; (b) Nyquist plots of Ni-$Co_9S_8$/rGN, Ni-$Co_9S_8$, $Co_9S_8$/rGN and NiS/$Ni_9S_8$/rGN; (c) The corresponding $R_{ct}$ values and equivalent circuit diagram (inset); (i) Chronoamperometry tests for Ni-$Co_9S_8$/rGN and Pt/C at 0.70 V, and chronopotentiometry tests for Ni-$Co_9S_8$/rGN and $RuO_2$ at 10 mA $cm^{-2}$.

On the basis of the excellent bi-functional electrocatalytic performance of Ni-$Co_9S_8$/rGN, a home-made Zn–air battery (Figure 6a) was assembled to evaluate the practical battery performance. Such battery exhibited high peak power density value of 171.5 mW $cm^{-2}$ at the current density of 310.0 mA $cm^{-2}$ (Figure 6b), which is much higher than Pt/C+$RuO_2$ composite (112.0 mW $cm^{-2}$ at 225.0 mA $cm^{-2}$), indicating the excellent property of Ni-$Co_9S_8$/rGN in practical Zn–air batteries. Additionally, the rate performance of charging/discharging processes measured separately in Figure 5c showed that the platform potential changed slightly by gradually increasing the operating current density. Result demonstrated that the existence of spatially hierarchical porous structure of Ni-$Co_9S_8$/rGN effectively facilitated the mass transfer of the battery. Since working stability is also a key parameter in practical battery operation, the durability test of Ni-$Co_9S_8$/rGN based Zn–air battery was conducted at current density of 10.0 mA $cm^{-2}$. As can be seen in Figure 6d, the Ni-$Co_9S_8$/rGN based Zn–air battery showed initial charge and discharge potential of 1.92 and 1.13 V with a voltage gap of 0.79 V, and also showed negligible change even over 120 h. In

comparison, the Pt/C+$RuO_2$ based battery displayed slight lower initial charge potential (1.88 V) and discharge potential (1.08 V) with a voltage gap of 0.80 V, a bit higher than Ni-$Co_9S_8$/rGN and moreover, suffered from severe decrease in durability. In comparison, the overall battery performance of Ni-$Co_9S_8$/rGN outperformed many reported Zn–air batteries in recent literatures (Table S3). Therefore, it is concluded that the Ni-$Co_9S_8$/rGN is promising in Zn–air battery application. The optical images in Figure 6e showed that all the LED (~3.0 V) decorated lights on the tree were successfully driven by two Zn–air batteries.

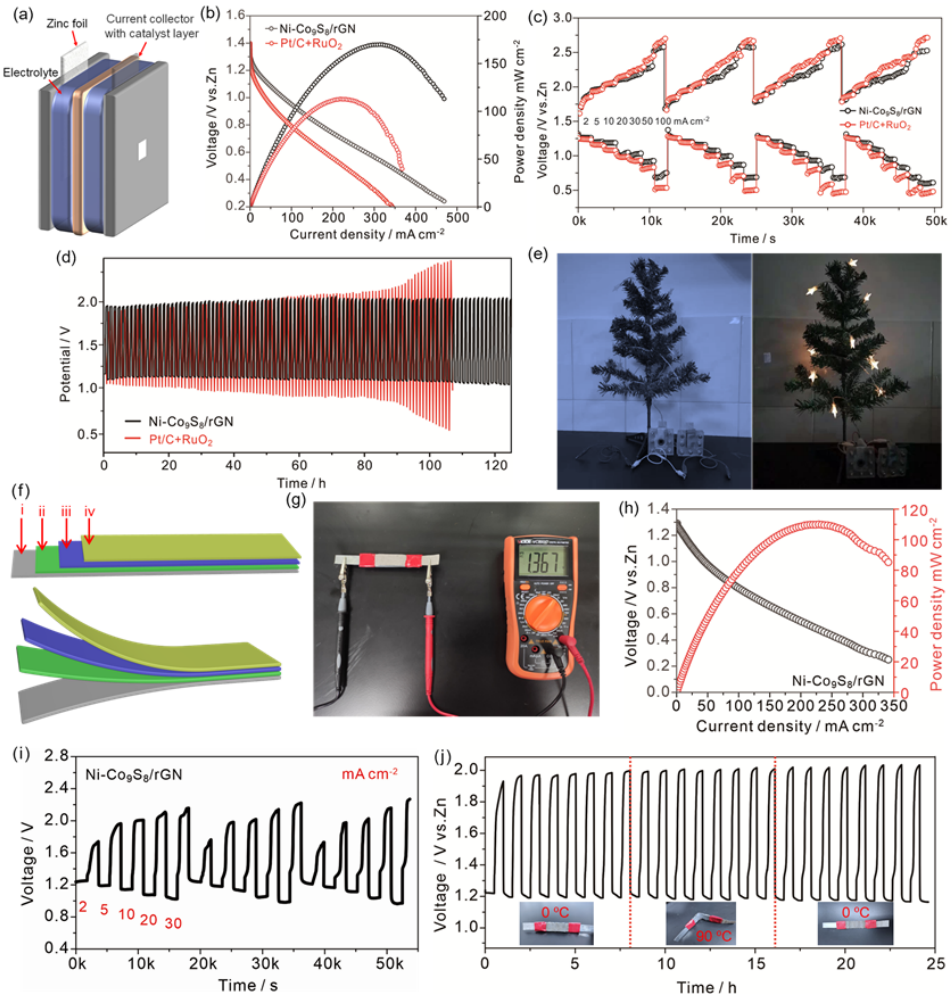


**Figure 6 The Zn–air battery performance of the as-prepared catalysts.** (a) Schematic of a home-made Zn–air battery; (b) LSV polarization and corresponding power density curves; Rate performance (c) and cycling stability (d) of Ni-$Co_9S_8$/rGN and Pt/C+$RuO_2$ based Zn-air batteries; (e) Optical images of a LED (~3.0 V) decorated tree before and after being driven by two Zn–air batteries. (f) Schematic illustration of the flexible Zn–air battery (i-iv are Zn foil, solid electrolyte, Ni-$Co_9S_8$/rGN, and Ni foil, respectively); (g) Open circuit potential image of a flexible battery; (h) The corresponding LSV and corresponding power density curves; (i) Rate performance of the batteries at different current densities; (j) Cycling stability of Ni-$Co_9S_8$/rGN at different bending degree.

In order to investigate the potential applications of Ni-$Co_9S_8$/rGN catalyst in wearable potential applications, an all-solid state Zn–air battery was constructed (Figure 6f) with an open circuit potential of approximately1.37 V (Figure 6g) and exhibits high power density of 110.0 mW $cm^{-2}$ at the current density of 223.0 mA $cm^{-2}$ (Figure 6h), indicating high application wearable potential of the sample. The rate performance in Figure 6i demonstrated that such a battery can be operated at both high (30 mA $cm^{-2}$ with voltage gap of 1.18 V) and low current density (2 mA $cm^{-2}$ with voltage gap of 0.55 V). The durability test was also conducted via the galvanostatic charge/discharge cycle at 1 mA $cm^{-2}$ with the different bending angle of the battery (Figure 6j). As a result, the Ni-$Co_9S_8$/rGN-based battery delivered a slight increase in the voltage gap after 25 h discharge/charge cycles, further demonstrating its superb cycling stability as a flexible electrode. Moreover, four of the devices together can successfully operate a 5.0 V bluetooth headset (Figure S19 and Video S1).

**Conclusion**

In summary, this work emphasizes the synergistic regulation of the intrinsic activities of ORR/OER and mass/electron transfer properties. In particular, rGN supported nickel-doped $Co_9S_8$ has been developed via a simple solvothermal procedure for the electrocatalysis of oxygen reduction/evolution reactions and Zn-air batteries. The spindle-type nanorod assembled Ni-$Co_9S_8$ sphere in Ni-$Co_9S_8$/rGN possessed hierarchical porous structure with uniform graphene nanoribbon coverage, which effectively shortened the ion diffusion pathway, expose more active sites, and accelerated the electron migration. Besides, the Ni-doping in the $Co_9S_8$ improved the intrinsic ORR/OER activities by optimizing the adsorption properties of oxygen species on the electrochemical interfaces. Due to the synergistic regulation of Ni-doping and rGN supported hierarchical porous structure, the Ni-$Co_9S_8$/rGN demonstrated an $\Delta E$ value of 0.65 V between OER and ORR, which is better than comparative samples, commercial $RuO_2$ and Pt/C. Moreover, as a bi-functional catalyst for

rechargeable and flexible Zn–air batteries, higher power density, superior rate performance and long-term cycling stability were achieved, providing new insights in high efficiency and low-cost oxygen-related bi-functional electrocatalyst development.

**Supporting Information**
Supporting Information is available from the Wiley Online Library or from the author.

**Acknowledgements**

This work is supported by the Research Foundation for Distinguished Scholars of Qingdao Agricultural University (665-1119008), the Opening Fund of Key Laboratory of Material Chemistry for Energy Conversion and Storage, Ministry of Education (2020JYBKF04), the Hong Kong Research Grants Council through the Early Career Scheme (Project No. 25301617) and the Hong Kong Polytechnic University grant (Project No. ZVRP). The authors would like to thank Dr. Wei Lu for optimizing the JEOL JEM-2100F microscope and also thank the Central Laboratory of Qingdao Agriculture University for the help in material characterization.

Received: ((will be filled in by the editorial staff))
Revised: ((will be filled in by the editorial staff))
Published online: ((will be filled in by the editorial staff))

**References**

[1] D. R. Rolison, J. W. Long, J. C. Lytle, A. E. Fischer, C. P. Rhodes, T. M. McEvoy, M. E. Bourg, A. M. Lubers, *Chem. Soc. Rev.* **2009**, *38*, 226.

[2] L. Li, Z. Wu, S. Yuan, X.-B. Zhang, *Energy Environ. Sci.* **2014**, *7*, 2101.

[3] Y. Huang, M. Zhu, Y. Huang, Z. Pei, H. Li, Z. Wang, Q. Xue, C. Zhi, *Adv. Mater.* **2016**, *28*, 8344.

[4] J. Yan, Y. Wang, Y. Zhang, S. Xia, J. Yu, B. Ding, *Adv. Mater.* **2021**, *33*, 2007525.

[5] Z. Cui, G. Fu, Y. Li, J. B. Goodenough, *Angew. Chem. Int. Ed.* **2017**, *56*, 9901.

[6] Y. Gu, G. Yan, Y. Lian, P. Qi, Q. Mu, C. Zhang, Z. Deng, Y. Peng, *Energy Stor. Mater.*

**2019**, *23*, 252.

[7] M. Liu, Z. Zhao, X. Duan, Y. Huang, *Adv. Mater.* **2019**, *31*, 1802234.

[8] L. Cao, Z. Zhao, Z. Liu, W. Gao, S. Dai, J. Gha, W. Xue, H. Sun, X. Duan, X. Pan, *Matter* **2019**, *1*, 1567.

[9] Y. Qiu, J. A. Lopez-Ruiz, U. Sanyal, E. Andrews, O. Y. Gutiérrez, J. D. Holladay, *Appl. Catal. B: Environ.* **2020**, *277*, 119277.

[10] A. Zagalskaya, V. Alexandrov, *ACS Catal*. **2020**, *10*, 3650.

[11] F. Lyu, Q. Wang, S. M. Choi, Y. Yin, *Small* **2019**, *15*, 1804201;

[12] D. Wang, S. Liu, J. Wang, R. Lin, M. Kawasaki, E. Rus, K. E. Silberstein, M. A. Lowe, F. Lin, D. Nordlund, *Nat. Commun.* **2016**, 7, 1.

[13] X.-T. Wang, T. Ouyang, L. Wang, J.-H. Zhong, Z.-Q. Liu, *Angew. Chem. Int. Ed.* **2020**, *59*, 6492.

[14] Z. Q. Liu, X. T. Wang, T. Ouyang, L. Wang, T. Ma, *Angew. Chem. Int. Ed* **2019**, *131*, 13425.

[15] J. Pan, X. L. Tian, S. Zaman, Z. Dong, H. Liu, H. S. Park, B. Y. Xia, *Batteries & Supercaps* **2019**, *2*, 336.

[16] Y. Zhu, X. Liu, S. Jin, H. Chen, W. Lee, M. Liu, Y. Chen, *J. Mater. Chem. A* **2019**, *7*, 5875.

[17] M. Chen, L. Wang, H. Yang, S. Zhao, H. Xu, G. Wu, *J. Power Sources* **2018**, *375*, 277.

[18] Y. Yang, R. Zeng, Y. Xiong, F. J. DiSalvo, H. D. Abruña, *J. Am. Chem. Soc.* **2019**, *141*, 19241;

[19] Y. Fan, S. Ida, A. Staykov, T. Akbay, H. Hagiwara, J. Matsuda, K. Kaneko, T. Ishihara, *Small* **2017**, *13*, 1700099.

[20] X. Wang, Q. Li, P. Shi, J. Fan, Y. Min, Q. Xu, *Small* **2019**, *15*, 1901530.

[21] Z.-Z. Liu, X. Shang, B. Dong, Y.-M. Chai, *J. Catal.* **2018**, *361*, 204.

[22] B. Yan, D. Krishnamurthy, C. H. Hendon, S. Deshpande, Y. Surendranath, V.

Viswanathan, *Joule* **2017**, *1*, 600.

[23] T.-F. Hung, Z.-W. Yin, S. B. Betzler, W. Zheng, J. Yang, H. Zheng, *Chem.Eng. J.* **2019**, *367*, 115.

[24] S. Ibraheem, S. Chen, J. Li, Q. Wang, Z. Wei, *J. Mater. Chem. A* **2019**, *7*, 9497.

[25] N. Zang, Z. Wu, J. Wang, W. Jin, *J. Mater. Chem. A* **2020**, *8*, 1799.

[26] X. Wang, P. He, Y. Yang, F. Zhang, J. Tang, R. Que, *Electrochim. Acta* **2020**, *345*, 136228.

[27] A. P. Tiwari, D. Kim, Y. Kim, H. Lee, *Adv. Energy Mater.* **2017**, *7*, 1602217.

[28] H. F. Wang, C. Tang, B. Wang, B. Q. Li, Q. Zhang, *Adv. Mater.* **2017**, *29*, 1702327.

[29] G. Fu, J. Wang, Y. Chen, Y. Liu, Y. Tang, J. B. Goodenough, J. M. Lee, *Adv. Energy Mater*. **2018**, *8*, 1802263.

[30] D. Dong, Z. Wu, J. Wang, G. Fu, Y. Tang, *J. Materials Chem. A* **2019**, *7*, 16068.

[31] Z. Wu, J. Wang, M. Song, G. Zhao, Y. Zhu, G. Fu, X. Liu, *ACS Appl. Mater. Interfaces* **2018**, *10*, 25415.

[32] S. Zhang, D. Zhai, T. Sun, A. Han, Y. Zhai, W.-C. Cheong, Y. Liu, C. Su, D. Wang, Y. Li, *Appl. Catal. B: Environ.* **2019**, *254*, 186.

[33] J. Yang, G. Zhu, Y. Liu, J. Xia, Z. Ji, X. Shen, S. Wu, *Adv. Funct. Mater.* **2016**, *26*, 4712.

[34] Y. Guo, L. Gan, C. Shang, E. Wang, J. Wang, *Adv. Funct. Mater.* **2017**, *27*, 1602699.

[35] Z. Wu, Y. Zhao, W. Jin, B. Jia, J. Wang, T. Ma, *Adv. Funct. Mater.* **2020**, 2009070.

[36] D. V. Kosynkin, A. L. Higginbotham, A. Sinitskii, J. R. Lomeda, A. Dimiev, B. K. Price, J. M. Tour, *Nature* **2009**, *458*, 872.

[37] J. Wang, Z. Wu, L. Han, R. Lin, W. Xiao, C. Xuan, H. L. Xin, D. Wang, *J. Mater. Chem. A* **2016**, *4*, 5678.

[38] J. Wang, H. L. Xin, J. Zhu, S. Liu, Z. Wu, D. Wang, *J. Mater. Chem. A* **2015**, *3*, 1601.

[39] Y. Guo, Q. Liu, Z. Li, Z. Zhang, X. Fang, *Appl. Catal. B: Environ.* **2018**, *221*, 362.

[40] T. Zhang, Z. Li, Z. Zhang, L. Wang, P. Sun, S. Wang, *J. Phys. Chem. C* **2018**, *122*, 27469.

[41] X. Han, Q. Chen, H. Zhang, Y. Ni, L. Zhang, *Chem. Eng. J.* **2019**, *368*, 513.

[42] M. S. Riaz, X. Yuan, Y. Zhao, C. Dong, S. Nong, Z. Ali, F. Huang, *Adv. Sustainable Syst.* **2019**, *3*, 1800167.

[43] X. Han, W. Zhang, X. Ma, C. Zhong, N. Zhao, W. Hu, Y. Deng, *Adv. Mater.* **2019**, *31*, 1808281.

[44] S. Piontek, C. Andronescu, A. Zaichenko, B. Konkena, K. Junge Puring, B. Marler, H. Antoni, I. Sinev, M. Muhler, D. Mollenhauer, *ACS Catal.* **2017**, *8*, 987.

[45] H. Yang, C. Wang, Y. Zhang, Q. Wang, *Small* **2018**, *14*, 1703273.

[46] H. Jin, J. Wang, D. Su, Z. Wei, Z. Pang, Y. Wang, *J. Am. Chem. Soc.* **2015**, *137*, 2688.

[47] Z. Wei, J. Wang, S. Mao, D. Su, H. Jin, Y. Wang, F. Xu, H. Li, Y. Wang, *ACS Catal.* **2015**, *5*, 4783.

[48] X. Li, K. Li, S. Zhu, K. Fan, L. Lyu, H. Yao, Y. Li, J. Hu, H. Huang, Y. W. Mai, *Angew. Chem. Int. Ed.* **2019**, *58*, 6239.

[49] Y. Tang, F. Jing, Z. Xu, F. Zhang, Y. Mai, D. Wu, *ACS Appl. Mater. Interfaces* **2017**, *9*, 12340.

[50] S. Mao, Z. Wen, T. Huang, Y. Hou, J. Chen, *Energy Environ. Sci.* **2014**, *7*, 609.

[51] J. K. Nørskov, J. Rossmeisl, A. Logadottir, L. Lindqvist, J. R. Kitchin, T. Bligaard, H. Jonsson, *J. Phys. Chem. B* **2004**, *108*, 17886.

Reduced-graphene-nanoribbon supported hierarchical porous nickel doped $Co_9S_8$ spheres shows high-efficiency oxygen reduction and evolution activities, and excellent rechargeable /flexible Zn-air battery performance because of the synergistic regulation between the uniform rGN covered hierarchical architecture and nickel dopants in promoting the intrinsic ORR/OER properties, electrical conductivity, and mass transfer.

Jie Wang, Jinxiao Xu, Xunyun Guo, Tao Shen, Cuijuan Xuan, Baoling Tian, Zhaorui Wen, Ye Zhu* and Deli Wang*

Synergistic Regulation of Nickel Doping/Hierarchical Structure in Cobalt Sulfide for High Performance Zinc-Air Battery

ToC figure